The Astrophysical Journal, 933:179 (14pp), 2022 July 10 https://doi.org/10.3847/1538-4357/ac745f

Effects of CO-dark Gas on Measurements of Molecular Cloud Stability and the Size–Linewidth Relationship

Theo J. O'Neill[1], Rémy Indebetouw[1,2], Alberto D. Bolatto[3], Suzanne C. Madden[4], and Tony Wong[5]
[1] Department of Astronomy, University of Virginia, Charlottesville, VA 22904, USA; oneill@virginia.edu
[2] National Radio Astronomy Observatory, 520 Edgemont Road, Charlottesville, VA 22903, USA
[3] Department of Astronomy, University of Maryland, College Park, MD 20742, USA
[4] AIM, CEA, CNRS, Université Paris-Saclay, Université Paris Diderot, Sorbonne Paris Cité, F-91191, Gif-sur-Yvette, France
[5] Department of Astronomy, University of Illinois, Urbana, IL 61801, USA
Received 2022 February 8; revised 2022 May 2; accepted 2022 May 26; published 2022 July 13

Abstract

Stars form within molecular clouds, so characterizing the physical states of molecular clouds is key to understanding the process of star formation. Cloud structure and stability are frequently assessed using metrics including the virial parameter and Larson scaling relationships between cloud radius, velocity dispersion, and surface density. Departures from the typical Galactic relationships between these quantities have been observed in low-metallicity environments. The amount of H_2 gas in cloud envelopes without corresponding CO emission is expected to be high under these conditions; therefore, this CO-dark gas could plausibly be responsible for the observed variations in cloud properties. We derive simple corrections that can be applied to empirical clump properties (mass, radius, velocity dispersion, surface density, and virial parameter) to account for CO-dark gas in clumps following power-law and Plummer mass density profiles. We find that CO-dark gas is not likely to be the cause of departures from Larson's relationships in low-metallicity regions, but that virial parameters may be systematically overestimated. We demonstrate that correcting for CO-dark gas is critical for accurately comparing the dynamical state and evolution of molecular clouds across diverse environments.

Unified Astronomy Thesaurus concepts: Molecular clouds (1072); Interstellar medium (847)

1. Introduction

Star formation is strongly correlated with tracers of molecular gas over kiloparsec scales (e.g., Kennicutt et al. 2007; Leroy et al. 2008; Bigiel et al. 2011), suggesting a causal relationship between the two. Since molecular clouds are the sites of star formation, understanding their dynamical states is necessary to accurately predict star formation, both in individual clouds as well as across larger populations.

Molecular hydrogen H_2 is the most abundant molecule in the interstellar medium (ISM) and is therefore closely tied to understanding the stability of molecular clouds and the process of star formation. H_2 is a symmetric homonuclear molecule, with widely spaced rotational energy levels and no permanent dipole moment; as a consequence of this, it radiates very weakly and is difficult to observe directly under conditions typical of molecular clouds ($T \sim 10$–20 K). It is therefore necessary to use more accessible molecules as tracers of H_2 to fully understand the conditions under which stars form.

CO is one of the next most abundant molecules in the ISM and can be easily excited at low temperatures, making it a popular tracer of H_2. Using CO as a tracer, the amount and spatial distribution of the molecular gas in a region is often used to infer the process of star formation; however, this use of CO as a proxy for H_2 relies on the assumption that it faithfully traces the full spatial extent of H_2. It is well known that some portion of the H_2 in molecular clouds is not traced by CO: since CO is less efficient at shielding itself from far-ultraviolet radiation than H_2 is, the transition from C^+ to CO occurs closer to the center of clouds than the transition from HI to H_2, resulting in a central CO-traceable region surrounded by an extended diffuse envelope of "CO-dark" H_2.

Recent studies have simulated the formation of H_2 and CO in the ISM to evaluate the expected amount of CO-dark H_2 in a variety of environments (e.g., Glover et al. 2010; Glover & Mac Low 2011; Gong et al. 2018; Li et al. 2018). Wolfire et al. (2010, hereafter W10) modeled photodissociation regions (PDRs) of individual spherical clouds and defined the fraction of molecular H_2 mass not traced by CO, or the "dark gas fraction," as

$$f_{\rm DG} = 1 - \frac{M(R_{\rm CO})}{M(R_{\rm H_2})}, \quad (1)$$

where $M(r)$ represents the mass contained within a radius r, $R_{\rm CO}$ is the radius of the CO-traceable material at which the optical depth, τ, equals 1 in the $J = 1$–0 transition, and $R_{\rm H_2}$ is the radius at which half of the hydrogen in the envelope surrounding the CO clump is molecular and half is atomic. This model is shown in Figure 1. Assuming standard Galactic conditions, W10 derived $f_{\rm DG} \sim 0.3$, a result that they found to be relatively insensitive to cloud and environmental properties. Other studies, both of individual cloud envelopes and at Galactic scales, have derived $f_{\rm DG} \sim 0.4$, but observed a stronger dependence on environmental properties (e.g., Smith et al. 2014; Szucs et al. 2016).

Similar values of $f_{\rm DG}$ have been found through observational work. In studies of individual Galactic clouds, f_{DG} has been found to be $\gtrsim$0.3 (e.g., Grenier et al. 2005; Abdo et al. 2010; Velusamy et al. 2010; Lee et al. 2012; Langer et al. 2014; Xu et al. 2016), and on Galactic scales CO-dark gas has been inferred to be 0.2–0.3 times as massive as the total atomic mass

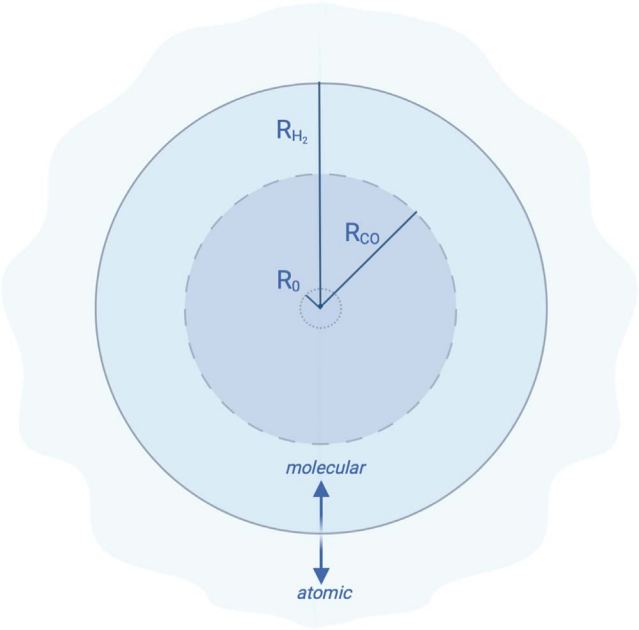

Figure 1. Clump toy model adapted from W10. R_{H_2} is the radius at which the densities of atomic and molecular hydrogen are equal. The gas within R_{H_2} is mostly molecular and the gas outside R_{H_2} is mostly atomic. R_{CO} is the radius at which CO-traced material has $\tau = 1$ in the J = 1–0 transition, and is a function of f_{DG}, with higher f_{DG} yielding smaller R_{CO}. R_0 is the normalizing radius and is typically typically $\ll R_{CO}$. For a pure power-law density profile (Section 2.1), R_0 is arbitrary, while for a power-law profile with a core (Section 2.2) or a Plummer profile (Section 2.3), it represents the radius of the flat central core.

of the Milky Way and 1.2–1.6 times as massive as its total CO-traced molecular mass (Planck Collaboration et al. 2011; Paradis et al. 2012).

The amount of CO-dark gas is expected to increase in high-radiation environments, with the $C^+/C^0/CO$ transition shifting even further into the cloud to reach higher overall column densities. Similarly, the dark-gas fraction is expected to increase in low-metallicity (low-Z) environments, where decreasing dust-to-gas ratios combine with typically stronger radiation fields to increase the efficiency of CO destruction (Madden et al. 2006; Gordon et al. 2011; Madden et al. 2020). H_2 can additionally be photodissociated via Lyman–Werner–band photons, but since it can be optically thick under some A_V conditions, it is able to remain self-shielded while CO is photodissociated. These effects have been supported observationally in the metal-poor outskirts of the Galaxy and in the Large and Small Magellanic Clouds (LMC and SMC, respectively, with $Z \sim 1/2\ Z_\odot$ and $Z \sim 1/5\ Z_\odot$), where $f_{DG} \gtrsim 0.8$ (Pineda et al. 2013; Jameson et al. 2018; Chevance et al. 2020).

Although much work has gone into quantifying the cause and amount of CO-dark gas in a variety of environments, the practical impact of this gas on interpretations of metrics of clump stability and evolution has not been explored in as much depth. Assessing the gravitational stability of clouds as measured by the virial parameter α_{vir} (Bertoldi & McKee 1992) or if clouds conform to "Larson's relationships" between cloud radius, velocity dispersion, and surface density (Larson 1981) is ubiquitous in both theoretical and observational studies. In low-Z environments, departures from the typical values and relationships between these quantities for CO clouds under Galactic conditions have been observed (e.g., Bolatto et al. 2008; Hughes et al. 2013; Rubele et al. 2015; Ochsendorf et al. 2017; Kalari et al. 2020). CO-dark gas could plausibly be responsible for these variations, since f_{DG} is known to be high in these regions, and cloud properties inferred from CO-traced material are not guaranteed to be representative of the overall state of the structures. Correcting for CO-dark gas may then be an essential step in evaluating the dynamical states and likely futures of molecular clouds across a range of environments.

Here, we present explicitly the variation in cloud properties from what would be inferred using CO-traceable material to the "true" state of clouds, including CO-dark gas. In Section 2, we summarize the mass density profiles that clouds may follow, derive corrections for empirical clump properties to account for CO-dark gas, and explore the behavior of α_{vir} as f_{DG} increases. We demonstrate the biases that CO-dark gas creates in interpretations of size–linewidth–surface density scaling relationships in Section 3. We discuss the implications of our results and the effects of CO-dark gas on star formation in Section 4, before concluding in Section 5.

2. Clump Density Profiles

Analyzing the stability of molecular clouds ($R \gtrsim 10$ pc), clumps ($R \sim 1$ pc), and cores ($R \lesssim 0.1$ pc) is of great interest to studies of their likely evolutionary futures. To this end, Bertoldi & McKee (1992) defined the virial parameter,

$$\alpha_{vir} = \frac{2\Omega_K}{|\Omega_G|} = \frac{M_{vir}}{M}, \tag{2}$$

as a measure of stability, where Ω_K is the kinetic energy, Ω_G is the gravitational potential energy, M is the structure's mass, and M_{vir} is its virial mass. $\alpha_{vir} < 1$ suggests that the structure is gravitationally dominated and rapidly collapsing, $\alpha_{vir} \sim 1$ indicates that a structure is gravitationally stable, and $\alpha_{vir} \gg 1$ suggests that a structure is subcritical and will likely expand, unless confined by external pressure.

Variations from the expected equilibrium values of α_{vir} have been observed in environments where f_{DG} is known to be high. In Galactic environments, α_{vir} is frequently $\lesssim 2$ (see Kauffmann et al. 2013 for a review) in clumps and clouds. In nearby low-Z dwarf galaxies and low-density, low-pressure environments, α_{vir} is frequently observed to be much larger, and can reach measured values of 4–10 or more (e.g., Schruba et al. 2017, 2019). Since these environments are rich in CO-dark gas, it is possible that the measured α_{vir} could be unrepresentative of the states of full clumps, and that this additional molecular reservoir is responsible for the variations in measured α_{vir}. Alternatively, these differences could also be explained by measurement errors in σ_v and R, stemming from large distance uncertainties, low-velocity resolutions, or varying definitions of cloud radius.

For all the clump density profiles that we will consider, we assume a one-dimensional radial velocity dispersion profile $\sigma_v(r)$ of

$$\sigma_v(r) = \left(\frac{r}{R_0}\right)^\beta \sigma_v(R_0), \tag{3}$$

where R_0 is a normalizing radius, as shown in Figure 1. When considered in combination with a non-constant-density profile $\rho(r)$, and if one considers turbulence to act as pressure support, our adopted Equation (3) leads to a gradient in energy density $\sim \rho\sigma_v^2$; we address the implications of this effect for cloud

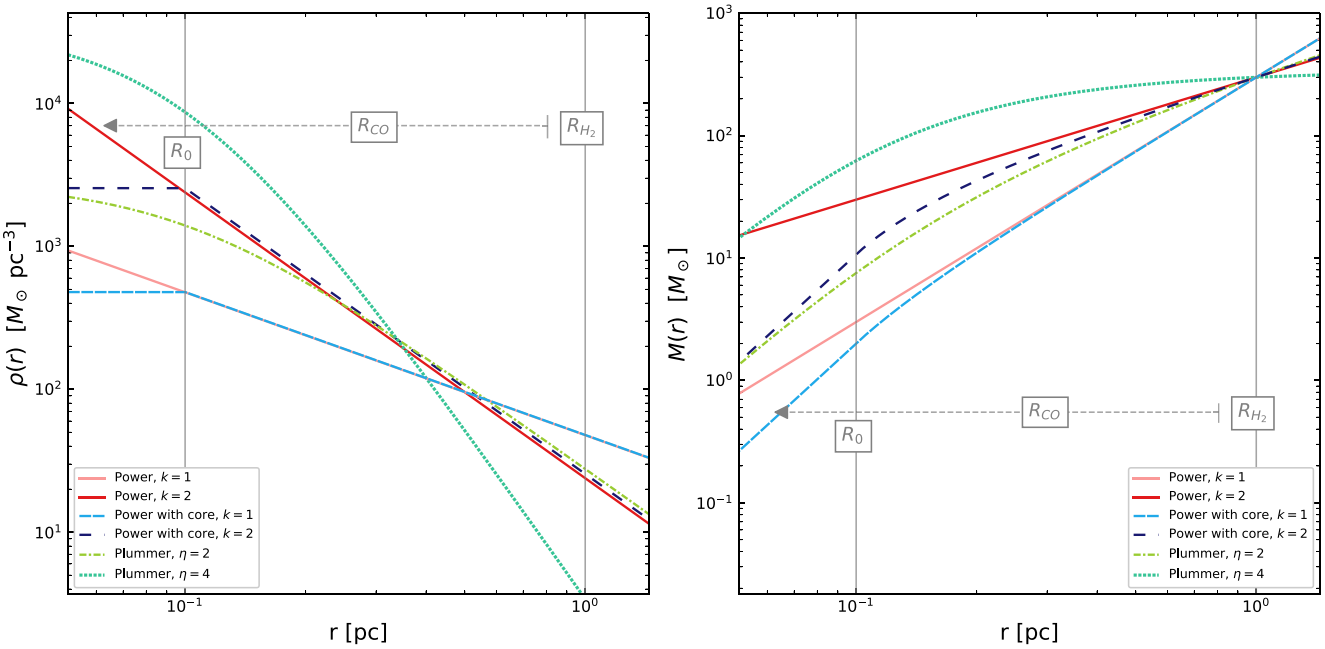

Figure 2. Left: density as a function of radius for a clump with [$R_0 = 0.1$ pc, $R_{H_2} = 1$ pc, $M(R_{H_2}) = 300\ M_\odot$, and $\sigma_v(R_{H_2}) = 0.6$ km s^{-1}]. R_0 and R_{H_2} are marked by the solid gray vertical lines, and the range of possible R_{CO} is shown by the dashed gray arrow. The solid pink and red curves are power-law profiles with $k = 1$ and $k = 2$, respectively (Section 2.1). The light blue densely dashed and dark blue loosely dashed curves are $k = 1$ and $k = 2$ power laws with constant-density cores, respectively (Section 2.2). The dashed–dotted yellow–green and dotted light green curves are Plummer density profiles with $\eta = 2$ and $\eta = 4$, respectively (Section 2.3). Right: total mass within r as a function of r for the fiducial clump, with the same line colors and styles as on the left.

stability in Section 4. Additionally, we recognize that at very small scales (∼0.1 pc), the effective pressure profile changes from thermal- to nonthermal-dominated support. Since the bulk of this work considers the effects of CO-dark gas on parsec scales, this behavior should not impact our conclusions.

We analyze how the observationally derived α_{vir} depends on the observed CO radius for clouds following a single power law (Section 2.1), a power law with a constant-density core (Section 2.2), and a Plummer profile (Section 2.3). We derive corrections for the empirical clump properties at a given dark-gas fraction f_{DG}. Finally, in Section 2.4, we compare the behaviors of the profiles considered and discuss the impact of the density profile on the effects of CO-dark gas.

2.1. Power-law Profile

Clouds are very frequently modeled as having a density profile $\rho(r)$, following a simple power-law,

$$\rho(r) = \rho_c\ x^{-k}, \tag{4}$$

where ρ_c is the central density, $x = r/R_0$, and R_0 is an arbitrary radius at which ρ is normalized. Figure 2 shows $\rho(r)$ and mass $M(r)$ as a function of r for a clump with properties [$R_0 = 0.1$ pc, $R_{H_2} = 1$ pc, $M(R_{H_2}) = 300\ M_\odot$, and $\sigma_v(R_{H_2}) = 0.6$ km s^{-1}], following $k = 1$ and $k = 2$.

In Appendix A.1, we derive the virial parameter for a clump following a power-law profile,

$$\alpha_{vir}(r) = \frac{3\sigma_v^2(r)}{\pi\rho_c G R_0^2}\frac{T_1(r)}{T_2(r)}, \tag{5}$$

where $T_1(r) = \left[\frac{4x^{(3-k)}}{(3-k)}\right]$ and $T_2(r) = \left[\frac{16x^{(5-2k)}}{(5-2k)(3-k)}\right]$. Figure 3 shows the variation of α_{vir} with r for the $k = 1$ and $k = 2$ profiles of the clump shown in Figure 2. We observe a large range of outcomes as r increases, depending on the velocity and power-law indices adopted. For [$k = 1$, $\beta = 0$], the cloud has a decreasing α_{vir} value as the radius increases, while for [$k = 1$, $\beta = 0.5$], α_{vir} is constant. Similarly, for [$k = 2$, $\beta = 0$], α_{vir} is constant, and for [$k = 2$, $\beta = 0.5$], α_{vir} increases with radius.

We then cast these equations in terms of W10's f_{DG} for more insight and to derive corrections to the observed molecular cloud properties for CO-dark gas. For a cloud following a power-law profile with $k < 3$, W10 defined

$$f_{DG} = 1 - \left(\frac{R_{CO}}{R_{H_2}}\right)^{3-k}. \tag{6}$$

We derive the variation in clump properties as a function of f_{DG}. Using the definition of f_{DG} in Equation (1), the total molecular mass within R_{H_2} can be found as

$$M(R_{H_2}) = \frac{M(R_{CO})}{1 - f_{DG}}. \tag{7}$$

From Equation (6), the relationship between R_{CO} and R_{H_2} is dependent on the adopted k,

$$R_{H_2} = (1 - f_{DG})^{1/(k-3)}\ R_{CO}, \tag{8}$$

and with Equation (3) evaluated at $R_0 = R_{CO}$, $\sigma_v(R_{H_2})$ can be found as

$$\sigma_v(R_{H_2}) = (1 - f_{DG})^{\beta/(k-3)}\ \sigma_v(R_{CO}). \tag{9}$$

Using Equations (6) and (7), surface density $\Sigma(r) = M(r)/\pi r^2$ at R_{H_2} becomes

$$\Sigma(R_{H_2}) = (1 - f_{DG})^{(1-k)/(k-3)}\ \Sigma(R_{CO}). \tag{10}$$

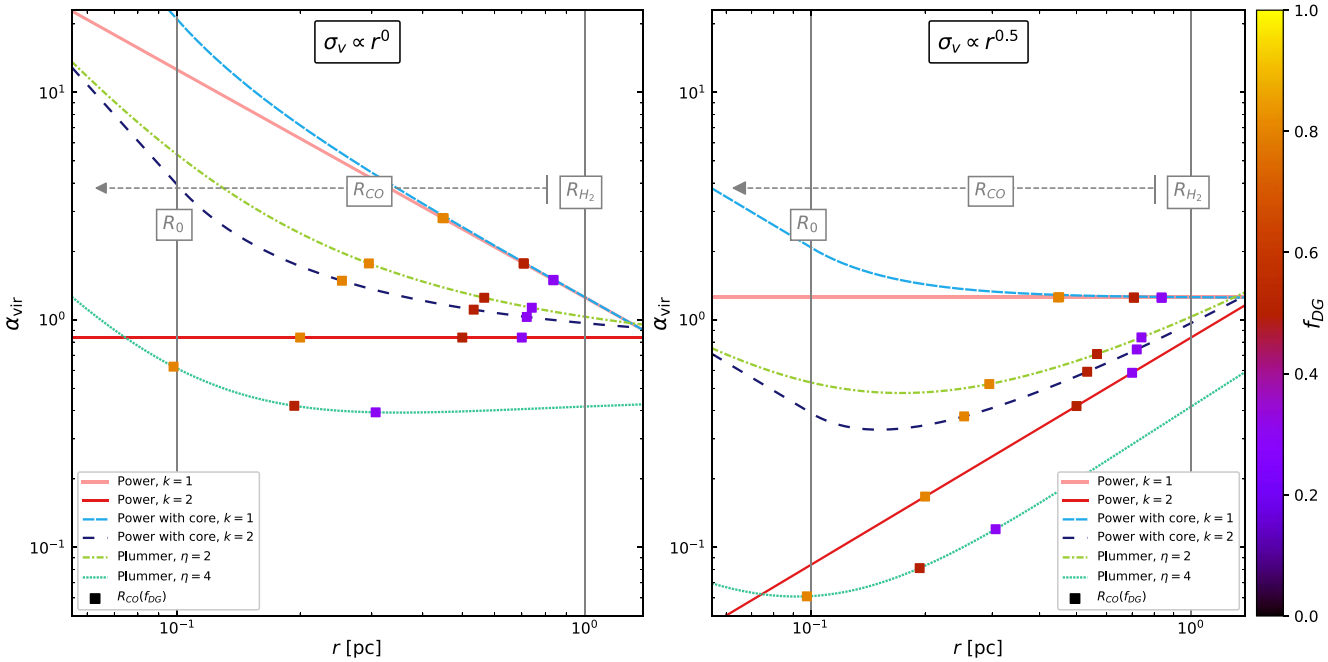

Figure 3. Left: the value of $\alpha_{\rm vir}$ vs. r for $\sigma_v \propto r^0$ [$\beta = 0$] for the clump shown in Figure 2, with [$R_0 = 0.1$ pc, $R_{\rm H_2} = 1$ pc, $M(R_{\rm H_2}) = 300\ M_\odot$, and $\sigma_v(R_{\rm H_2}) = 0.6$ km s^{-1}]. The colors and styles of the profile curves, the R_0 and $R_{\rm H_2}$ lines, and the $R_{\rm CO}$ arrow are the same as in Figure 2. The square points along each curve mark the location of $R_{\rm CO}$ for that profile by value of f_{DG}. The purple points mark $f_{\rm DG} = 0.3$, the red points mark $f_{\rm DG} = 0.5$, and the orange points mark $f_{\rm DG} = 0.8$. Right:the same as the left panel, but for $\sigma_v \propto r^{0.5}$ [$\beta = 0.5$].

The virial mass can be expressed in terms of $f_{\rm DG}$ as

$$M_{\rm vir}(R_{\rm H_2}) = (1 - f_{\rm DG})^{(2\beta+1)/(k-3)}\ M_{\rm vir}(R_{\rm CO}). \tag{11}$$

Finally, the CO-dark-corrected virial parameter is

$$\alpha_{\rm vir}(R_{\rm H_2}) = \alpha_{\rm vir}(R_{\rm CO})\ (1 - f_{\rm DG})^{(2\beta+k-2)/(k-3)}. \tag{12}$$

In Figure 3, we show the values of $R_{\rm CO}$ and $\alpha_{\rm vir}(R_{\rm CO})$ as a function of $f_{\rm DG}$ for the fixed $R(H_2) = 1$ pc clump: for $f_{\rm DG} = 0.3$, $R_{\rm CO} \simeq$ [0.85 pc for $k = 1$, 0.7 pc for $k = 2$], while for $f_{\rm DG} = 0.5$, $R_{\rm CO} \simeq$ [0.7 pc for $k = 1$, 0.5 pc for $k = 2$], and for $f_{\rm DG} = 0.8$, $R_{\rm CO} \simeq$ [0.45 pc for $k = 1$, 0.2 pc for $k = 2$].

We consider internal pressure for the power-law profile. Under a polytropic model, turbulent pressure within a cloud is described by $P \sim \rho\sigma_v^2$. By Equations (3) and (4), the pressure gradient for this profile then follows $dP/dx \sim (2\beta - k)x^{2\beta-k-1}$. Thus, if $2\beta - k < 0$, an outward pressure gradient conducive to stability will be present throughout the clump. Additionally, from Equation (12), we see that while $2\beta + k < 2$, $\alpha_{\rm vir}(R_{\rm H_2}) < \alpha_{\rm vir}(R_{\rm CO})$, i.e., the empirical $\alpha_{\rm vir}$ from the CO-traced clump would overestimate the "true" $\alpha_{\rm vir}$ of the full cloud including CO-dark gas. In this case, relying on the CO-derived measurement alone would lead to the incorrect conclusion that the cloud is dominated by kinetic energy, and is either unbound or confined by high levels of external pressure.

2.2. Power-law Profile with a Constant-density Core

We also examine a cloud profile that follows a power law at large r, but has a small, constant-density core of radius R_0 at its center,

$$\rho(r) = \begin{cases} \rho_c \text{ for } r < R_0 \\ \rho_c\ x^{-k} \text{ for } r \geqslant R_0, \end{cases} \tag{13}$$

where ρ_c is the central density and $x = r/R_0$. This has frequently been supported observationally, with $R_0 \lesssim 0.1$ pc (e.g., Girichidis et al. 2011; Juvela et al. 2018; Tang et al. 2018). We note that for this profile, unlike for the full power-law profile of Section 2.1, R_0 has a definite physical meaning, and that R_0 is typically $\ll R_{\rm CO}$. In Figure 2, $\rho(r)$ and $M(r)$ are shown for $k = 1$ and $k = 2$ for a clump with an identical set of properties at $R_{\rm H_2}$ to the clump considered in Section 2.1 [$R_0 = 0.1$ pc, $R_{\rm H_2} = 1$ pc, $M(R_{\rm H_2}) = 300\ M_\odot$, and $\sigma_v(R_{\rm H_2}) = 0.6$ km s^{-1}]. The densities of this profile and those of the full power-law profile described in Section 2.3 are roughly in agreement at about 0.5 pc; this is a consequence of the choice of R_0 and $R_{\rm H_2}$, and changing their values changes this radius of agreement. In Appendix A.2, we follow the process outlined in Section 2.1 to derive the virial parameter for this profile:

$$\alpha_{\rm vir}(r) = \begin{cases} \frac{15\sigma_v^2(r)}{4\pi\rho_c G R_0^2}\frac{1}{x^2} \text{ for } r < \mathrm{R_0} \\ \frac{3\sigma_v^2(r)}{\pi\rho_c G R_0^2}\frac{\Pi_1(r)}{\Pi_2(r)} \text{ for } r \geqslant \mathrm{R_0}, \end{cases} \tag{14}$$

where $\Pi_1(r) = \left[\frac{4}{3-k}\left(x^{3-k} - \frac{k}{3}\right)\right]$ and

$$\Pi_2(r) = \begin{cases} \frac{16}{3-k}\left(\frac{x^{5-2k}-1}{5-2k} + \frac{k(1-x^{2-k})}{6-3k} + \frac{3-k}{15}\right) \text{ for } k \neq 2 \\ \frac{16}{3-k}\left(\frac{x^{5-2k}-1}{5-2k} - \frac{k\ln(x)}{3} + \frac{3-k}{15}\right) \text{ for } k = 2. \end{cases} \tag{15}$$

The variation of $\alpha_{\rm vir}$ with r is shown in Figure 3 for $k = 1$ and $k = 2$. We observe a wide variety of behaviors as the area considered outside of the central core R_0 increases depending on the assumed density and velocity profiles. For both [$k = 1$, $\beta = 0$] and [$k = 2$, $\beta = 0$], $\alpha_{\rm vir}$ decreases rapidly with increasing x. For [$k = 1$, $\beta = 0.5$], $\alpha_{\rm vir}$ plateaus marginally below the value of $\alpha_{\rm vir}$ at $x = 1$, and for [$k = 2$, $\beta = 0.5$], it increases rapidly. Any conclusions as to whether the virial

parameter of the CO-traceable material accurately represents the entire cloud, including CO-dark gas, are then extremely dependent on the assumptions made.

In Appendix A.2, we also derive

$$f_{\rm DG} = \begin{cases} 1 - \left(\frac{3-k}{3} \frac{(R_{\rm CO}/R_0)^3}{(R_{\rm H_2}/R_0)^{(3-k)} - \frac{k}{3}} \right) \text{for } {\rm R_{CO}} < {\rm R_0} \\ 1 - \left(\frac{(R_{\rm CO}/R_0)^{(3-k)} - \frac{k}{3}}{(R_{\rm H_2}/R_0)^{(3-k)} - \frac{k}{3}} \right) \text{for } {\rm R_{CO}} \geqslant {\rm R_0}, \end{cases} \quad (16)$$

assuming $R_{\rm H_2} > R_0$. We show the value of $R_{\rm CO}$ as a function of $f_{\rm DG}$ in Figure 3 for $f_{\rm DG} = 0.3$, 0.5, and 0.8. For $f_{\rm DG} = 0.3$, $R_{\rm CO} \simeq$ [0.85 pc for $k = 1$, 0.7 pc for $k = 2$], while for $f_{\rm DG} = 0.5$, $R_{\rm CO} \simeq$ [0.7 pc for $k = 1$, 0.5 pc for $k = 2$], and for $f_{\rm DG} = 0.8$, $R_{\rm CO} \simeq$ [0.45 pc for $k = 1$, 0.25 pc for $k = 2$].

We consider the limit of a clump with a very large central core, such that R_0 approaches $R_{\rm H_2}$ and k is effectively zero throughout the clump. In this case, we can derive a simplified kinetic term, $\Omega_k \propto x^{2\beta+3}$, and gravitational term, $\Omega_G \propto x^5$, leading to

$$\alpha_{\rm vir} \propto x^{2\beta-2}. \quad (17)$$

Therefore, while $\beta < 1$, the virial parameter will decrease as the radius r at which the clump properties are evaluated increases. Most measurements of β on $\gtrsim$0.1 pc scales range between 0.2–0.5 (e.g., Caselli & Myers 1995; Heyer & Brunt 2004; Lin et al. 2022), so this condition appears to be easily met. We then expect that, if this condition should be met, a full clump including CO-dark gas would have a lower $\alpha_{\rm vir}$ than the result derived only from the CO-traced material, i.e., it would be more gravitationally dominated than could be inferred from CO alone.

2.3. Plummer Profile

The Plummer density profile (Plummer 1911) is frequently applied to molecular clouds and yields a small, flat inner core that transitions to a power-law profile at large radii. The Plummer profile follows

$$\rho(r) = \rho_c \left(\frac{1}{\sqrt{x^2+1}} \right)^{\eta}, \quad (18)$$

where ρ_c is the central density, R_0 is the radius of the central core, $x \equiv r/R_0$, and η is the index of the power law at large radii. Pattle (2016) modeled the evolution of pressure-confined cores following Plummer-like density profiles in order to evaluate whether the cores were likely to collapse or reach virial equilibrium as a function of radius. Here, we extend this work in the context of CO-dark gas.

We derive corrections for CO-dark gas for two values of η: $\eta = 2$, as consistent with recent observational results ranging between $\eta = 1.5$–2.5 (e.g., Arzoumanian et al. 2011; Palmeirim et al. 2013; Zucker et al. 2021), and $\eta = 4$, following Whitworth & Ward-Thompson (2001) and Pattle (2016). We adopt an internal cloud velocity dispersion profile following Equation (3). $\rho(r)$ and $M(r)$ are shown in Figure 2 for the fiducial clump with properties [$R_0 = 0.1$ pc, $R_{\rm H_2} = 1$ pc, $M(R_{\rm H_2}) = 300\ M_\odot$, and $\sigma_v(R_{\rm H_2}) = 0.6$ km s^{-1}].

In Appendix A.3, we derive the virial parameter for this profile as

$$\alpha_{\rm vir}(r) = \frac{3\sigma_v^2(r)}{\pi \rho_c G R_0^2} \frac{P_1(r)}{P_2(r)}, \quad (19)$$

where

$$P_1(r) = \begin{cases} 4(x - \arctan(x)) \text{ for } \eta = 2 \\ 2(\arctan(x) - \frac{x}{x^2+1}) \text{ for } \eta = 4, \end{cases} \quad (20)$$

and

$$P_2(r) = \begin{cases} 4P_1(r) - 16 \int_0^x \frac{x' \arctan(x')}{x'^2+1} {\rm d}x' \text{ for } \eta = 2 \\ \arctan(x) + \frac{x - 4\arctan(x)}{x^2+1} + \frac{2x}{(x^2+1)^2} \text{ for } \eta = 4. \end{cases} \quad (21)$$

We similarly derive

$$f_{\rm DG} = \begin{cases} 1 - \left(\frac{\frac{R_{\rm CO}}{R_0} - \arctan(R_{\rm CO}/R_0)}{\frac{R_{\rm H_2}}{R_0} - \arctan(R_{\rm H_2}/R_0)} \right) \text{for } \eta = 2 \\ 1 - \left(\frac{\arctan(R_{\rm CO}/R_0) - \frac{(R_{\rm CO}/R_0)}{(R_{\rm CO}/R_0)^2+1}}{\arctan(R_{\rm H_2}/R_0) - \frac{(R_{\rm H_2}/R_0)}{(R_{\rm H_2}/R_0)^2+1}} \right) \text{for } \eta = 4. \end{cases} \quad (22)$$

In Figure 3, we present the behavior of $\alpha_{\rm vir}$ as a function of r for this profile. We also numerically solve for and plot the expected $R_{\rm CO}$ using Equation (22) for $f_{\rm DG} = 0.3$, 0.5, and 0.8. For $f_{\rm DG} = 0.3$, $R_{\rm CO} \simeq$ [0.75 pc for $\eta = 2$, 0.3 pc for $\eta = 4$]. For $f_{\rm DG} = 0.5$, $R_{\rm CO} \simeq$ [0.55 pc for $\eta = 2$, 0.2 pc for $\eta = 4$], and for $f_{\rm DG} = 0.8$, $R_{\rm CO} \simeq$ [0.3 pc for $\eta = 2$, 0.1 pc for $\eta = 4$].

As in the other profiles considered, the behavior of $\alpha_{\rm vir}$ for the Plummer profile is highly variable and is dependent upon the density and velocity assumptions made. For a cloud with $\beta = 0$, $\alpha_{\rm vir}$ is roughly constant for $x > 1$ and only marginally below the value of $\alpha_{\rm vir}$ at $x = 1$. This indicates that the stability that would be inferred from just the CO-traced mass is a fairly accurate representation of the stability of the entire cloud. In contrast, for $\beta = 0.5$, $\alpha_{\rm vir}$ increases rapidly above R_0, suggesting that the CO-traced cloud would appear more gravitationally bound than the full cloud at $R_{\rm H_2}$.

2.4. Comparison of Density Profiles

We consider the effect of the density profile on $\alpha_{\rm vir}$ and the amount by which CO-dark gas changes the observed clump properties. The impact of k/η on the overall value of $\alpha_{\rm vir}$ is similar between all the profiles considered, with smaller k leading to higher $\alpha_{\rm vir}$ below $R_{\rm H_2}$. In particular, $\alpha_{\rm vir}$ is typically $\sim$2 times larger for the power-law profiles of Sections 2.1 and 2.2 than the $\alpha_{\rm vir}$ of the $\eta = 4$ Plummer profile. This is the result of the $\eta = 4$ Plummer profile having a much higher proportion of mass centrally concentrated at small r than the $k = 1$ and $k = 2$ power-law-based profiles and the $\eta = 2$ Plummer profile (see Figure 2).

Since $\Omega_G \sim GM^2/r$, concentrating a fixed amount of mass within a smaller area increases the object's gravitational potential and decreases the virial mass. In contrast, $\Omega_K \sim \sigma_v^2 M$ is not as dependent on the volume in which M is contained, so it is unsurprising that $\alpha_{\rm vir}$ is significantly reduced for the steeper profiles. Very subvirial clumps are expected to rapidly collapse, and so to offset this effect and move closer to

stability at R_{H_2}, the Plummer profile would need to have a much higher $\sigma_v(R_{H_2})$. The assumed radial velocity dispersion index β also has a large impact on clump dynamical state and the α_{vir} that would be inferred after correcting for CO-dark gas. For all the profiles considered in this section, the choice of β generally corresponds to the "direction" of the behavior of α_{vir} with r, whether increasing, decreasing, or constant.

Throughout this work, we use f_{DG} for a given clump as a set parameter, without attempting to tie its specific value to the underlying physics that determine the value of f_{DG}. In reality, f_{DG} is a function of the properties of the clump and the environment in which it is immersed. Since we aim to derive corrections that may be applied by observers using a specific assumed or measured value of f_{DG} to estimate clump properties, accounting for the nuances of the physical drivers of f_{DG} is beyond the scope of this work. However, we do expect that clumps with steeper density profiles will have lower f_{DG} than clumps with shallower profiles occupying the same environment under identical conditions.

We can intuitively consider that, in a given environment, a specific A_V/density threshold must be reached for CO to effectively self-shield (as determined by radiation field strength, dust-to-gas ratio, etc). Since steeper profiles are more centrally concentrated in mass, they would contain a larger fraction of the total clump mass at this density floor, where CO begins to be destroyed (R_{CO}); this would decrease f_{DG}, despite being in an identical environment to a shallower clump.

Finally, we evaluate the overall effect of the internal density profile assumed for inferred CO-dark-corrected clump properties. For the fixed R_{H_2} we consider, the derived R_{CO} for a given f_{DG} decreases with increasing k (or η) because of our assumption that $R_0 \ll R_{CO}$. The values of R_{CO} and $\alpha_{vir}(R_{CO})$ for a power law with core profile with $k = 1$ are functionally identical to those for a full power law, and for a $k = 2$ power law with core profile they depart only slightly from the values derived from a full $k = 2$ power law. Under most scenarios where $R_0 \ll R_{CO}$, the corrected properties (R_{H_2}, $\alpha_{vir}(R_{H_2})$, etc.) derived for the power law with core profile vary by a small amount (generally $\lesssim$10 % difference) from the corrections for a full power law. The difference in the corrected properties between profiles increases with increasing f_{DG}. The difference in the corrected values between the steep $\eta = 4$ Plummer and power law profiles is larger, but this is more likely to be an effect of the variation in assumed η versus k than of profile itself; the $\eta = 2$ profile also typically differs by $\lesssim$10 % from the power-law-based profiles.

Therefore, we conclude that the relative steepness by which density decreases with r has a larger impact on the effects of CO-dark gas on observed clump properties than the exact form of the radial density profiles that we consider. For the remainder of this work, we focus our analysis on the behavior of clumps following single power-law profiles, for simplicity.

3. CO-dark Gas and Size–Linewidth–Surface Density Relationships

3.1. Larson's Scaling Relationships

Larson (1981) observed correlations between the size R, velocity dispersion σ_v, and mass surface density Σ of Galactic molecular clouds, which have been confirmed and refined by later studies. The first of these relationships is a power-law relationship between the size of a cloud R and σ_v, where

$$\sigma_v \simeq C \left(\frac{R}{1\ \mathrm{pc}}\right)^{\Gamma} \mathrm{km\ s^{-1}}. \quad (23)$$

Larson (1981) originally derived $\Gamma = 0.38$ and $C = 1.1$ km s^{-1}, an estimate that Solomon et al. (1987) and Heyer et al. (2009; hereafter SRBY and H09, respectively) later refined to

$$\sigma_v \simeq 0.72 \left(\frac{R}{1\ \mathrm{pc}}\right)^{0.5} \mathrm{km\ s^{-1}}. \quad (24)$$

Larson's second relationship is derived from observed correlations between σ_v and cloud mass M,

$$\frac{2\sigma_v^2 R}{GM} \simeq 1, \quad (25)$$

which is usually interpreted as meaning that most clouds are roughly in virial equilibrium. Alternatively, it has been suggested that this is a signature of global hierarchical collapse at all scales within clouds (Ballesteros-Paredes et al. 2011; Vázquez-Semadeni et al. 2019). Finally, cloud density and size are observed to be inversely related, $n \propto R^{-1.1}$, suggesting that surface density is independent of size and should be roughly constant for clouds under conditions similar to the Milky Way, although observations have suggested that Σ does vary over several orders of magnitude with environment (e.g., H09; Sun et al. 2018; Traficante et al. 2018; Dessauges-Zavadsky et al. 2019; Chevance et al. 2020).

As noted by H09, a natural extension of these relationships is an association between surface density Σ and the size–linewidth parameter σ_v^2/R. A virialized sphere following a power-law density distribution should follow

$$\frac{\sigma_v^2}{R} = \frac{(3-k)}{3(5-2k)} \pi G \Sigma. \quad (26)$$

In Figures 4 and 5, we compare the relationships between R, σ_v, and Σ for structures observed using CO as a tracer across a variety of environments:

1. Galactic giant molecular clouds (GMCs), with subsamples with areas defined from ^{12}CO by SRBY and from the ^{13}CO half-power contours of their central cores (H09);
2. Clouds in the Galactic central molecular zone (Oka et al. 2001);
3. Cores observed in the Ophiuchus molecular cloud (Ridge et al. 2006);
4. Cores in the Perseus molecular cloud (Shetty et al. 2012);
5. Clumps in the Magellanic Bridge (Kalari et al. 2020; Valdivia-Mena et al. 2020);
6. Clumps in the LMC regions 30 Doradus, A439, GMC 104, GMC 1, PCC, and N59C (Wong et al. 2019);
7. GMCs in ~150 star-forming regions throughout the LMC (Ochsendorf et al. 2017); and
8. Clouds in the SMC and dwarf galaxy IC 10 (Bolatto et al. 2008)

(where the choice of core/clump/cloud terminology corresponds to commonly used size scales of ~0.1/1/10 pc, without any differences in the relevant physics being implied).

In Figure 4, where R and σ_v are compared, the usual size–linewidth relationship of Equation (24) is displayed. Σ and

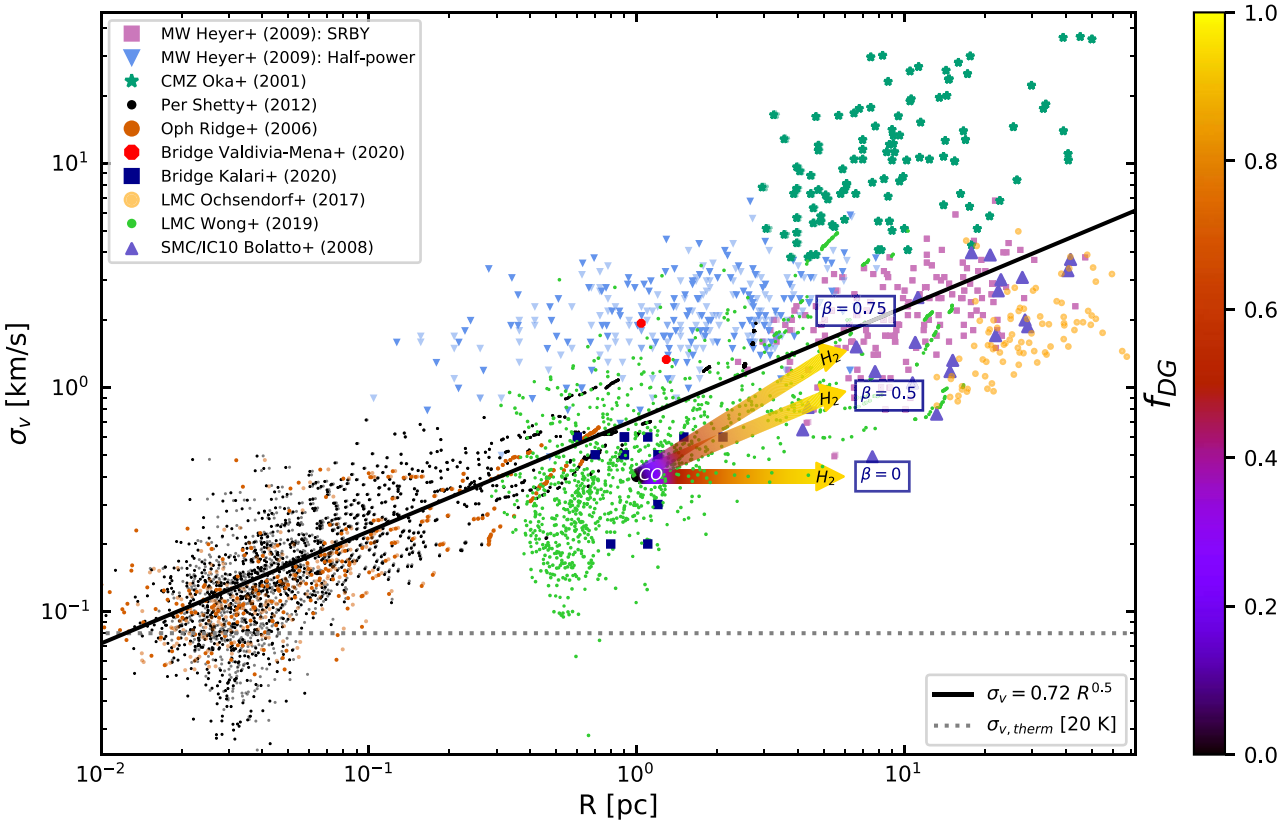

Figure 4. Velocity dispersion σ_v compared to radius R of the CO-traced structures described in Section 3. The black line follows the relationship $\sigma_v = 0.72R^{0.5}$ (Equation (24)) and the gray dotted line shows the expected contribution from thermal motion to σ_v at $T = 20$ K. The arrows show the direction in which one would correct the observed CO-traced clump properties for CO-dark gas to recover the properties of the full H_2 clump. The arrows start at physical properties typical of parsec-scale CO-traced clumps, and move toward the inferred properties of the H_2 clump. Each arrow is labeled with the power-law index k and velocity dispersion index β assumed to generate its path, and the color gradient along the arrows shows the corrected H_2 properties as a function of f_{DG}.

σ_v^2/R are compared in Figure 5 for a subset of the sources listed above that have cloud mass estimates derived without assuming virial equilibrium (1, 6, 7, and 8 in the list above). Equation (26) is shown as the straight black line for $k = 0$. Additionally, in pressure-bounded virial equilibrium, Σ and σ_v^2/R are related as (Field et al. 2011)

$$\frac{\sigma_v^2}{R} = \frac{1}{3}\left(\pi\gamma G\Sigma + \frac{4P_e}{\Sigma}\right), \tag{27}$$

which is shown in Figure 5 by the V-shaped curves, with $\gamma = 0.6$ for a cloud with $k = 0$.

The majority of the Wong et al. (2019) and Ochsendorf et al. (2017) LMC GMCs, the Kalari et al. (2020) Bridge clumps, and the Bolatto et al. (2008) SMC and IC 10 clouds have smaller σ_v for a given R than expected from Galactic clouds, falling well under the relationship described in Equation (24). This has been observed in a variety of other low-Z environments as well, e.g., by Rubio et al. (2015) in the $Z \simeq 0.13\,Z_\odot$ dwarf galaxy Wolf–Lundmark–Melotte, and by Hughes et al. (2013) in the LMC. Many of these samples also have lower Σ for a given σ_v^2/R than expected, based on Equation (26), suggesting that the structures are either unbound and transient or must be confined by external pressure to remain stable, as position in this space is directly related to α_{vir}.

As part of the Physics at High Angular resolution in Nearby GalaxieS with ALMA collaboration (PHANGS, Leroy et al. 2021), Sun et al. (2020) analyzed the dynamical states of molecular gas in 28 nearby disk galaxies. They derived typical midplane pressures over 1 kpc scales ranging from $P/k_B = 10^3$–10^6 K cm^{-3}, and found that the average internal turbulent pressure of clouds was typically very similar to the required cloud-scale equilibrium pressure, which they concluded indicated that most gas was in dynamical equilibrium. Wong et al. (2009) derived an average midplane hydrostatic pressure in the central regions of the LMC of $P/k_B \sim 10^4$ K cm^{-3} using HI and CO(1–0) observations, which could be sufficient to confine a large fraction of the Wong et al. (2019) LMC clumps observed to have high σ_v^2/R, as well as the majority of the Ochsendorf et al. (2017) LMC GMCs.

3.2. Effects of CO-dark Gas on Observed Relationships

The effects of our derived corrections for CO-dark gas in a power-law density profile clump (Section 2.1: Equations (8), (9), and (10)) are shown by the arrows in Figures 4 and 5. The arrows start at the properties of a clump observed solely in CO, and move toward the "true" characteristics of the full clump, including CO-dark gas, with color gradients along the arrow corresponding to f_{DG}. The initial conditions for the corrections displayed are [$R_{CO} = 1$ pc, $\sigma_v(R_{CO}) = 0.4$ km s^{-1}, and $M(R_{CO}) = 35\,M_\odot$]; these values correspond to the medians of these quantities for roughly parsec-scale CO clumps in the Wong et al. (2019) sample. Changing the arrow's origin does not impact the direction of the arrow. In Figure 4(a), we only show corrections for $k = 1$, with arrows for $\beta = 0$, $\beta = 0.5$, and $\beta = 0.75$; this is because the corrections for $k = 1$ versus $k = 2$

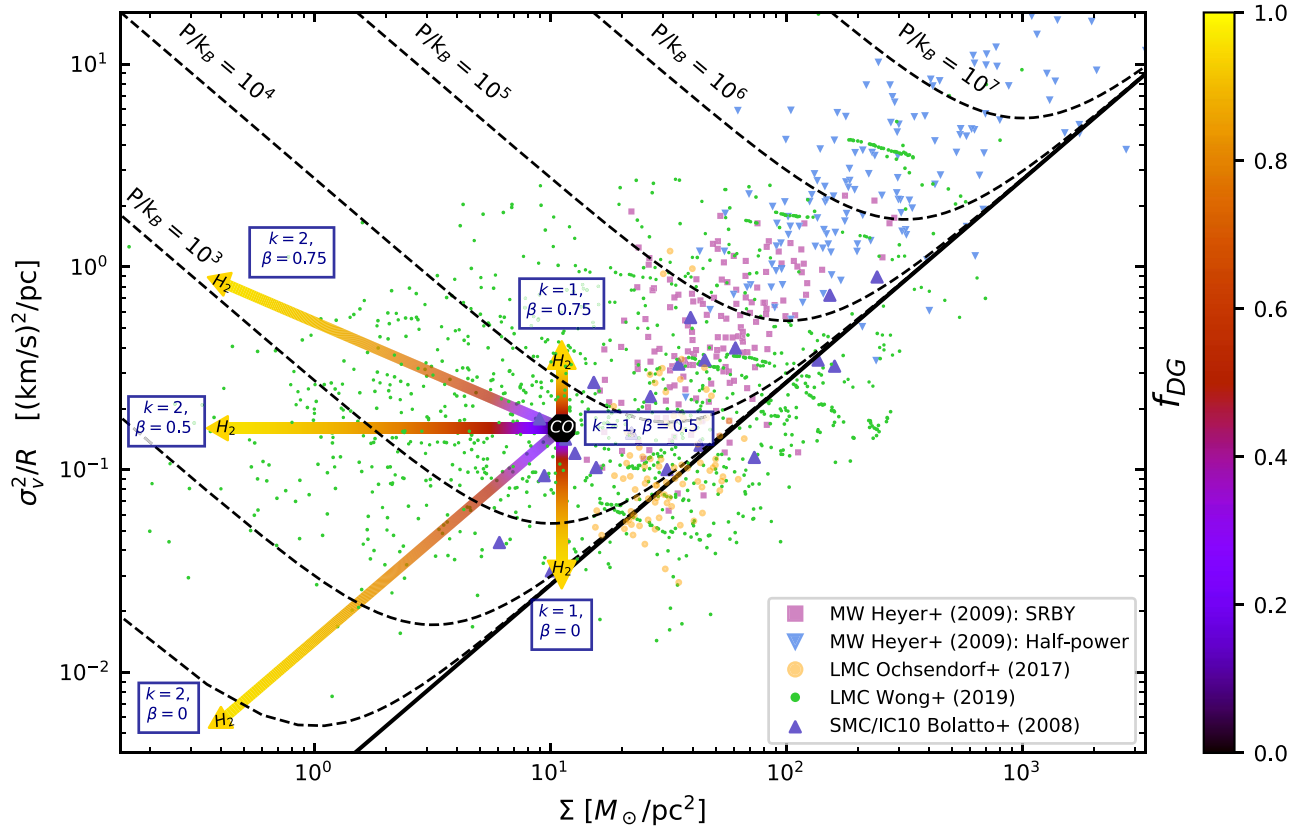

Figure 5. Size–linewidth parameter σ_v^2/R compared to surface density Σ for the CO-traced structures described in Section 3. The black line corresponds to virial equilibrium without external pressure (Equation (26)), and the dashed black curves correspond to virial equilibrium under external pressure, with units for the P/k_B labels in K cm^{-3} (Equation (27)). The arrows are as in Figure 4 and show the direction in which one would correct the observed CO-traced clump properties to recover the properties of the full clump, including CO-dark H_2.

overlap in this space and differ only in the extent to which their arrows extend. In Figure 5, we also show corrections for $k = 2$.

For $\beta = 0$, correcting for CO-dark gas causes clumps to have even lower σ_v relative to the increased R and thus drives the clumps farther from following Equation (24). We note that a velocity profile this "flat" is unlikely, as turbulence within the ISM is mainly driven at large scales (Brunt et al. 2009), but we display it to demonstrate the limits of this effect. For $\beta = 0.5$, the corrections have no effect on the position of the clump in size–linewidth space relative to the expected Equation (24) relationship; this is because the standard interclump relationship (Equation (24)) and the displayed intraclump profile share the same $\beta = \Gamma = 0.5$. By the same logic, $\beta = 0.75$ unsurprisingly brings clumps closer to agreement with Equation (24), because $\beta > \Gamma$. Corrections in Σ versus σ_v^2/R space have a similarly variable effect. The distance of any given clump from the virial line in Figure 5 is directly proportional to the stability of the clump as measured by $\alpha_{\rm vir}$, and we interpret the corrections for a power-law profile in this context as follows.

1. We again see that the assumed k and β have a large impact on the inferred corrected state: for $k = 1$, Σ is constant; while for $k > 2$, the corrected Σ is significantly reduced.
2. We observe that clumps decrease in $\alpha_{\rm vir}$ and move toward $\alpha_{\rm vir} \sim 1$ in all cases where $k + 2\beta < 2$. This suggests that if these profile conditions are met, the apparently high $\alpha_{\rm vir}$ structures traced by CO in low-Z, high-$f_{\rm DG}$ environments may be closer to stability than expected.
3. In most cases, the updated clump positions suggest that a lower level of external pressure would be required to maintain stability than would be inferred from CO-traced material alone.

The assumed density and velocity profiles then almost entirely determine the "direction" of these biases. This highlights the importance of studies of the spatial dependence of density and linewidth on the scale of individual clouds in addition to SRBY/H09-type studies comparing these quantities between cloud populations.

4. Discussion

4.1. Can CO-dark Gas Explain Departures from Larson's Relationships?

From the clump property corrections derived in Section 2 and described in Section 3, it is clear that neglecting CO-dark gas could significantly bias the assessment of cloud placement in Larson's relationships and gravitational stability. We now examine if this effect is sufficient to explain the observed high $\alpha_{\rm vir}$ and departures from Larson's relationships in low-Z environments.

Under the corrections for a power-law profile that we have derived, low-σ_v clumps must follow an internal velocity profile with $\beta > 0.5$ (i.e., have large motions at large scales) to reconcile with the typical size–linewidth relationship described by Equation (24); however, large βs also yield increased $\alpha_{\rm vir}$ that imply that the full structure is gravitationally unbound. If,

instead, one assumes that clouds are close to virialized without external pressure, then the dark-gas correction required to move the observed points closer to virialization (i.e., to decrease $\alpha_{\rm vir}$) requires that clumps follow a shallow density profile and have $\beta < 0.5$—but shallow βs increase the amount by which these clouds fall "under" the R–σ_v relationship of Equation (24).

This contradiction is most problematic in structures with high $f_{\rm DG}$, as expected in low-Z or high-radiation environments, and can be resolved if the clouds in these areas are: (1) overwhelmingly gravitationally unstable and dispersing rapidly as a result; or (2) require much higher levels of external pressure to remain stable than clouds in more typical environments; or (3) possess a global σ_v/R trend shifted to lower values of σ_v than the classical Equation (24) relationship (i.e., a smaller scaling coefficient C in Equation (23)) and have shallow internal density and σ_v profiles ($0 \leqslant \beta < 0.5$).

(1) is unlikely statistically, simply because of the number of clouds that are observed, and a physical cause for (2) is hard to imagine, since the typical ISM pressure in low-Z galaxies is ∼1–2 orders of magnitude smaller than in typical large spiral galaxies (de los Reyes & Aennicutt 2019). There are also nontrivial direct relationships between metallicity and ISM pressure in these areas, because of reduced cooling and thermal balance, but predictions as a function of metallicity are generally only possible in the context of a self-regulated star formation model, and thus the specifics depend on the details of that model. Additionally, the direct effects of metallicity via the cooling rate on pressure are less important than the galaxy type to the properties of molecular clouds.

(3) is then the most compelling, and would be the simplest way to account for the observed low-σ_v and high-$\alpha_{\rm vir}$ structures in low-Z areas. Shallow density profiles of $1.5 < k < 2$ are typical on the parsec scales where the simplified isolated spherical PDR model that we consider here holds (Caselli et al. 2002; Pirogov 2009; Arzoumanian et al. 2011; Schneider et al. 2013), and even shallower profiles ($k \sim 1$) have been found in young low-density cores and clumps (Chen et al. 2019, 2020; Lin et al. 2022). Small values of C and steep Γ relative to SRBY's $C = 0.72$ and $\Gamma = 0.5$ have been derived from CO observations for structures in the SMC, LMC, and other local dwarf galaxies where low-σ_v/high-$\alpha_{\rm vir}$ structures are found (with $C \sim 0.2$–0.6 and $\Gamma \sim 0.55$–0.85; Bolatto et al. 2008; Hughes et al. 2010, 2013; Wong et al. 2019). In CO-dark regions, HI can also be used as a probe of turbulence. For a sample of HI clouds in the LMC, Kim et al. (2007) derived a mean $\Gamma \simeq 0.5$.

In the pioneering Larson (1981) study, a shallow $\Gamma = 0.38$ was derived, which is similar to the Kolmogorov index for turbulent cascade in an incompressible medium $\beta \sim 1/3$. More recently, $\beta \simeq 1/2$ has frequently been found for GMCs, both observationally and through simulations (e.g., Heyer & Brunt 2004; Dobbs 2015); this aligns the expectation for Burgers turbulence (Passot et al. 1988), i.e., in an isotropic system dominated by shocks, and is in accordance with SRBY's $\Gamma = 0.5$. On very small scales ($\lesssim$0.05 pc), a break in the internal size–linewidth relationship has been observed with β approaching zero (Goodman et al. 1998; Caselli et al. 2002; Volgenau et al. 2006; Pineda et al. 2010); however, it seems unlikely that the W10 scenario of the PDRs of isolated individual spherical clouds being surrounded by envelopes of dark gas would hold on these sizes, because cores are typically embedded within larger structures.

Shallow values of β ($\beta \sim 0.2$–0.3) have also been derived in high-mass star-forming regions (Caselli & Myers 1995) and in prestellar cores and young clumps (Tatematsu et al. 2004; Lee et al. 2015; Lin et al. 2022). Bertram et al. (2015) analyzed turbulence within simulated molecular clouds using the Δ-variance method, from which they compared the values of β within the full cloud, within H_2 gas, and within CO-traced material. For initial densities ranging between 30–100 cm^{-3}, the derived β ranged between ∼0.3–0.6, as derived from the resulting H_2 density maps, and ∼0.15–0.4, as traced by CO density, a difference that they attributed to the compact nature of the CO structures as compared to the more extended H_2.

We emphasize that the interclump size–linewidth relationship with exponent Γ is obtained by comparing populations of clumps, while the intraclump size–linewidth relationship with exponent β is obtained by studying individual structures. The latter relationship is much more challenging to measure in typically distant low-Z environments, due to the required high angular resolutions, and it has only recently become possible, but is key for assessing if the implied shallow β is realistic. Overall, the measurements of β that have been obtained locally generally resemble the observed values of Γ.

This observed correspondence of $\beta \sim \Gamma \simeq 0.5$ has been interpreted as reflecting the uniformity of velocity structure functions between individual clouds, so that Γ is largely set by β (Heyer & Brunt 2004). The implication from (3) that β is shallower than the observed Γ in low-Z environments creates some tension with this conclusion. One explanation for this difference could be a correlation between f_{DG} and cloud size. In their sample of LMC GMCs, Ochsendorf et al. (2017) observed a decrease in the ratio of CO-traced mass to dust-traced mass, as the dust-traced mass increased. Since the dust-traced mass likely includes the diffuse CO-dark gas, this suggests that a correlation between $f_{\rm DG}$ and cloud size exists, with larger clouds having higher $f_{\rm DG}$. Larger clouds would then systematically have larger relative changes between their true properties including CO-dark gas and their observed properties than smaller clouds do.

The "true" Γ relating the full clouds including CO-dark gas could then be shallower than the observed, CO-derived Γ, and instead approach (and possibly be determined by) the expected shallow β. This would explain the general steepness of the CO-traced Γ in low-Z environments, as well as resolve the implied difference between β and Γ in low-Z environments. It is of course also possible that the clumps in these low-Z environments do truly have different physical properties and scaling relationships than clumps under Galactic conditions.

4.2. CO-dark Gas and Star Formation

4.2.1. Star Formation Efficiency Considering CO-dark Gas

On kiloparsec scales, low-Z galaxies have been found to depart from the Kennicutt–Schmidt relationship, possessing higher star formation rate (SFR) densities at a given molecular gas surface density as assessed by CO than found in more typical environments (e.g., Galametz et al. 2009; Schruba et al. 2012). Star formation efficiency (SFE) is frequently assessed by comparing the SFR to the gas mass ($\epsilon' = {\rm SFR}/M_{\rm cloud}$), so this departure suggests that the SFE is also much higher than under Galactic conditions.

Madden et al. (2020) showed that CO-dark gas is sufficient to cause the apparent variation from the Kennicutt–Schmidt

relationship on Galactic scales, and that when it is corrected for the missing mass star formation in these environments, it is not significantly more efficient. It has also been suggested that H_2 gas is not a requirement for star formation, but that it is usually present as a consequence of the necessary shielding for stars to form (Glover & Clark 2012; Krumholz 2012). Star formation could then in principle proceed in atomic gas without the presence of molecular gas (although this would be rare), and may explain the lack of CO detections and corresponding high implied SFEs in some low-Z star-forming galaxies.

While CO-dark gas appears to be responsible for increased SFEs on large scales, because surface densities averaged over large scales are increased by the addition of CO-dark gas mass, it is unclear how it impacts star formation in individual clumps. SFE is also frequently evaluated by simply comparing the total stellar mass to the total molecular mass ($\epsilon = M_*/M_{\rm cloud}$), or as a function of freefall time ($\epsilon_{ff} = \tau_{ff} \times \epsilon'$). A simple but perhaps naive correction to the SFE of an individual CO-traced clump for missing H_2 mass would be $\epsilon_{\rm H_2} = (1 - f_{\rm DG})\epsilon_{\rm CO}$, by Equation (7), with a similar correction for ϵ'. We have shown that CO-based observations are likely to overestimate the mean clump density. This would lead to underestimates of freefall time τ_{ff} and also, depending on the density profile, potentially lead to underestimates of ϵ_{ff} as well.

However, the ϵ-based metrics are generally derived over larger scales, which helps offset the unknown variation from the original total gas mass for any given star-forming clump to its present-day mass by averaging over clumps and cores at a variety of stages in the star formation process. Using the present-day gas mass of a single clump to try to derive a by-clump efficiency loses this advantage, and so we only suggest the use of the proposed corrected $\epsilon_{\rm H_2}$ and related quantities on larger scales, and even then with caution.

It is still not well understood if the actual way and timescale over which clouds collapse in low-Z environments is different than under conditions similar to the solar neighborhood; and, if so, how this departure influences the SFR/SFE. Parmentier (2020) and Parmentier & Pasquali (2020) derived a relationship between the clump radial density profile and the SFR and found that steeper profiles correspond to higher initial SFRs: star formation proceeds most rapidly in the densest areas of clumps, and the centers of clumps with very steep density profiles are denser than shallower clumps of the same mass.

Since radiation fields are known to be enhanced in the interclump medium, due to the decreased dust-to-gas ratios, it is plausible that the typical radial profiles of clumps could be different than in higher-Z environments. We have shown that shallow density profiles are required for the properties of low-Z clumps to approximate those of Galactic clumps, so it follows that in this scenario the low-Z clump-scale SFR could be slower than in higher-Z environments. To reconcile this with the observed high SFR averaged over kiloparsec scales, relatively more clumps would need to exist to achieve these values.

Measurements of the total gas mass and SFR over large scales are clearly critical for these observations of SFE, and it is well understood that underestimating the total mass can skew SFE estimates. An additional factor involves the mechanics of how these clouds collapse to form stars at clump and core scales, and the fraction of gas at these scales that actively contributes to star formation. The extent to which diffuse CO-dark envelopes participate in star formation is unclear and is one of several contributing factors that sets SFE.

The scaling relationships between molecular gas and SFR observed over large scales can be validated by understanding the fraction of gas at clump scales involved in star formation and the factors that affect the stability of individual cores and clumps. Detailed studies of the distribution and state of clumpy molecular gas will be key to fully explaining the SFR/SFE and origin of scaling relationships at kiloparsec scales. Our models show the importance of the CO-dark gas fraction and the density and velocity dispersion profiles in influencing these properties. This work is then relevant to large-scale measurements of SFEs in contextualizing interpretations of these measurements.

4.2.2. Relationship between $f_{\rm DG}$ and the CO-to-H_2 Conversion Factor

The corrections for CO-dark gas that we have derived are dependent on having an estimate of the total molecular gas within $R_{\rm CO}$, which could be derived through, e.g., assuming local thermal equilibrium (LTE) with the use of multiple CO transitions or applying non-LTE RADEX modeling or similar methods. The widely used CO-to-H_2 conversion factor,

$$X_{\rm CO} = \frac{N({\rm H_2})}{I_{\rm CO}} [{\rm cm^{-2}\ (K\ km\ s^{-1})^{-1}}]$$
$$\alpha_{\rm CO} = \frac{M_{\rm vir}(R_{\rm CO})}{L_{\rm CO}}\ [M_\odot\ ({\rm K\ km\ s^{-1}\ pc^2})^{-1}], \quad (28)$$

is also designed to account for the untraced H_2 gas that we correct for in this work using $f_{\rm DG}$. Some degree of correspondence between the two is then expected, as shown in previous works simulating the relationship between $X_{\rm CO}$ and environmental conditions (Shetty et al. 2011a, 2011b; Clark & Glover 2015; Szucs et al. 2016; Gong et al. 2018, 2020).

To demonstrate this expected relationship in the context of this work, we define a crude mass ratio factor Y_{DG}, where

$$Y_{\rm DG} = \frac{M(R_{\rm H_2})}{M(R_{\rm CO})} = \frac{1}{1 - f_{\rm DG}}, \quad (29)$$

by Equation (1). To compare the value of Y_{DG} across different environments, we define $Y_{DG,MW}$ as the typical value of Y_{DG} in the $f_{DG,MW}$ Milky Way. The expected Y_{DG} in a given environment can then be compared to $Y_{DG,MW}$ through the ratio of their respective f_{DG},

$$Y_{\rm DG} = \left(\frac{1 - f_{DG,MW}}{1 - f_{\rm DG}}\right) Y_{DG,MW}. \quad (30)$$

For a typical $Z \sim 1\,Z_\odot$ Galactic environment with $f_{DG,MW} = 0.3$ (W10), $Y_{DG,MW} \simeq 1.4$. From this value, $Y_{\rm DG} \simeq 3.5\,Y_{DG,MW}$ would be expected in an environment like the $Z = 0.2\,Z_\odot$ SMC with $f_{\rm DG} \sim 0.8$ (Jameson et al. 2018). This corresponds very well to the observed ratio between the usual Galactic $X_{CO,MW}$ and $X_{\rm CO}$ derived in SMC clumps: for subparsec clumps in the SMC Wing, Muraoka et al. (2017) derived $X_{\rm CO} \sim 4\ X_{\rm CO,MW}$, and for parsec-scale clumps in the Magellanic Bridge, Kalari et al. (2020) derived $X_{\rm CO} \sim 3\ X_{\rm CO,MW}$ and Valdivia-Mena et al. (2020) found $X_{\rm CO} \sim 1.5$–$3.5\ X_{\rm CO,MW}$. This suggests that Y_{DG} (and $f_{\rm DG}$) could be used as a check of the measured $X_{\rm CO}$ in clumps, or vice versa. In contrast, measurements of $X_{\rm CO}$ over cloud scales and larger ($\gtrsim$10 pc) in the SMC have ranged between 20–50 $X_{\rm CO,MW}$ (Leroy et al. 2009; Bolatto et al. 2011; Jameson et al. 2016),

significantly exceeding the ratio between Y_{DG} and $Y_{DG,MW}$ that we have derived here.

This variation between the X_{CO} and Y_{DG} estimates is likely caused by the well-known limits of X_{CO} at small scales (see Bolatto et al. 2013 for a review) and the limits of f_{DG} as formulated for isolated spherical PDRs by W10/in this work at large scales. When at low metallicities, X_{CO} is expected and observed to increase rapidly. On cloud and global scales, X_{CO} measurements are averaged over many clouds and so include both diffuse and dense molecular gas. For individual low-Z/high-f_{DG} clumps, though, only dense gas is reflected.

The scale (and resolution) at which clumps are measured is negatively associated with derived X_{CO}: in the LMC, for example, Fukui et al. (2008) derived $X_{CO} \sim 4\,X_{CO,MW}$ from clouds observed at ~40 pc resolution by NANTEN, while Hughes et al. (2010) derived $X_{CO} \sim 2\,X_{CO,MW}$ from structures observed at ~10 pc resolution by the Magellanic Mopra Assessment survey. Lower-resolution observations run the risk of small clumps being diluted by large beam sizes, artificially inflating α_{vir} and X_{CO}, and also increasing the likelihood of such clumps not being identified at all. Resolved observations of individual parsec-scale clumps in distant low-Z environments have only recently become possible and typically yield smaller conversion factors (Muraoka et al. 2017; Schruba et al. 2017; Saldaño et al. 2018; Kalari et al. 2020; Valdivia-Mena et al. 2020), approaching $X_{CO,MW}$ and in alignment with our expectations for clump f_{DG}.

4.3. Guidance for Interpreting Observations

We present the case of a "typical" observed CO clump with high α_{vir}, and discuss the properties that would be inferred by an observer using our derived corrections for CO-dark gas. For a clump following a typical $k = 1.5$ and $\beta = 0.5$ with [R_{CO} = 1 pc, $\sigma_v(R_{CO}) = 0.4$ km s^{-1}, $M(R_{CO}) = 35\,M_\odot$, and $\alpha_{vir}(R_{CO}) = 4.3$], a moderate Galactic $f_{DG} \sim 0.3$ (W10) yields a relatively small difference in clump properties: [$R_{H_2} = 1.3$ pc, $\sigma_v(R_{H_2}) = 0.45$ km s^{-1}, $M(R_{H_2}) = 50\,M_\odot$, and $\alpha_{vir}(R_{H_2}) = 4.8$]. In contrast, an extreme $f_{DG} \sim 0.9$, as occasionally derived in low-Z environments (Jameson et al. 2018), would lead to a significantly different set of inferred properties: [$R_{H_2} = 4.6$ pc, $\sigma_v(R_{H_2}) = 0.86$ km s^{-1}, $M(R_{H_2}) = 350\,M_\odot$, and $\alpha_{vir}(R_{H_2}) = 9.2$].

We then see that under typical assumed clump density and velocity profiles, correcting for CO-dark gas does *not* resolve the apparent instability of the structure—it actually exacerbates the issue. We emphasize again that the changes in clump properties post-correction are highly dependent upon the choice of k and β; if the same clump followed shallower profiles, a reduction in α_{vir} could just as easily be indicated. At the same time, the magnitude of this shift makes clear that correcting for CO-dark gas is essential for an accurate assessment of clump properties in high-f_{DG} environments.

5. Conclusions

We have derived easily applied corrections to CO-derived clump properties to account for the effects of CO-dark gas. Our main conclusions are as follows:

1. For molecular clouds following power-law or Plummer density profiles, CO-derived measurements will systematically underestimate cloud mass and size. If clumps have shallow mass density and radial velocity dispersion profiles, the virial parameter α_{vir} will be overestimated (Section 2).
2. In order to interpret CO observations as accurately as possible, cloud properties (e.g., size, mass, surface density, velocity dispersion, and virial parameter) should be corrected using the prescriptions outlined in Section 2, as demonstrated in Section 4.3.
3. CO-derived measurements are most suspect in low-Z, high-f_{DG} regions; however, CO-dark gas is unlikely to simultaneously be the cause of observed clumps with high α_{vir} and low σ_v relative to Larson's relationships in low-Z environments (Sections 3, 4.1).

Understanding what other processes might drive departures from Larson's relationships and from inferred virial equilibrium should be of high priority. Attempts to correct for all of the above effects are reliant on the accurate assessment of intracloud density and velocity profiles, and so this too should continue to be prioritized, especially on clump scales.

It is clear that assessing how star formation proceeds within clumps in low-Z regions is dependent on understanding the impact of CO-dark gas. Accounting for CO-dark gas on both local and global scales is then key to evaluating the evolutionary history and likely future of specific regions and to placing star formation in low-Z environments into its correct context. The corrections that we have presented here are one tool for better leveraging CO observations to estimate clump behavior after accounting for the effects of environment.

We thank Kelsey Johnson, Allison Costa, and Molly Finn for useful comments and discussion. T.J.O. and R.I. were supported during this work by NSF award 2009624. T.W. acknowledges support from NSF AAG award 2009849. The National Radio Astronomy Observatory is a facility of the National Science Foundation, operated under cooperative agreement by Associated Universities, Inc. This paper makes use of the following ALMA data: ADS/JAO.ALMA#2012.1.00683.S, ADS/JAO.ALMA#2015.1.01013.S, and ADS/JAO.ALMA #2016.1.00193.S. ALMA is a partnership of ESO (representing its member states), NSF (USA), and NINS (Japan), together with NRC (Canada), MOST and ASIAA (Taiwan), and KASI (Republic of Korea), in cooperation with the Republic of Chile. The Joint ALMA Observatory is operated by ESO, AUI/NRAO, and NAOJ.

Software: Astropy (Astropy Collaboration et al. 2013, 2018); BioRender (https://biorender.com); Matplotlib (Hunter 2007); Numpy (Harris et al. 2020).

Appendix
Derivation of Clump Density Profiles

For a clump following a given density profile $\rho(r)$, the relevant terms for calculating the virial parameter and corrections for CO-dark gas that we derive are as follows. The mass within a radius r can be found as

$$M(r) = 4\pi \int_0^r r'^2 \rho(r') dr'. \tag{A1}$$

This leads to gravitational potential energy

$$\Omega_G(r) = -4\pi G \int_0^r r'\, \rho(r') M(r') dr', \tag{A2}$$

where G is the fundamental gravitational constant. We assume a one-dimensional radial velocity dispersion profile $\sigma_v(r)$, following Equation (3). The total kinetic energy can be found as

$$\Omega_K(r) = \frac{3}{2} M(r)\sigma_v^2(r), \tag{A3}$$

and the virial mass $M_{\rm vir}(r)$ follows from requiring $2\Omega_K(r) = -\Omega_G(r)$.

A.1. Power-law Profile

We consider a clump following a power-law profile,

$$\rho(r) = \rho_c\, x^{-k}, \tag{A4}$$

where ρ_c is the central density, $x = r/R_0$, and R_0 is an arbitrary radius at which ρ is normalized. From Equation (A1), the mass of such a structure is

$$M(r) = \pi\rho_c R_0^3 T_1(r), \tag{A5}$$

where $T_1(r) = \left[\frac{4x^{(3-k)}}{(3-k)}\right]$. From Equation (A2), the gravitational term is

$$\Omega_G(r) = -\pi^2\rho_c^2 G R_0^5 T_2(r) = -\frac{GM(r)^2}{R_0}\frac{T_2(r)}{T_1(r)^2}, \tag{A6}$$

where $T_2(r) = \left[\frac{16x^{(5-2k)}}{(5-2k)(3-k)}\right]$. (The use of $T_1(r)$ and $T_2(r)$ in these expressions will make the parallels with subsequent radial density profiles clearer.) From Equation (A3), the kinetic term is

$$\Omega_K(r) = \frac{3}{2}\pi\rho_c R_0^3 T_1(r)\sigma_v^2(r). \tag{A7}$$

Requiring $2\Omega_K = -\Omega_G$, we derive the virial mass

$$M_{\rm vir}(r) = \frac{3\sigma_v^2(r)R_0}{G}\frac{T_1(r)^2}{T_2(r)}, \tag{A8}$$

which is equivalent to the classical virial mass definition (SRBY; MacLaren et al. 1988):

$$M_{\rm vir}(r) = \frac{3(5-2k)}{(3-k)}\frac{r\ \sigma_v^2(r)}{G}. \tag{A9}$$

From Equation (2), the virial parameter is then

$$\alpha_{\rm vir}(r) = \frac{3\sigma_v^2(r)}{\pi\rho_c G R_0^2}\frac{T_1(r)}{T_2(r)}, \tag{A10}$$

which is equivalent to

$$\alpha_{\rm vir}(r) = \frac{3(5-2k)}{4\pi\rho_c}\frac{\sigma_v^2(R_0)}{G}x^{2\beta+k-2}, \tag{A11}$$

under the scaling of the velocity dispersion profile of Equation (3).

In their Appendix A, W10 derived the dark-gas fraction for a power-law density profile with $k < 3$ as

$$f_{\rm DG} = 1 - \left(\frac{R_{\rm CO}}{R_{H_2}}\right)^{3-k}. \tag{A12}$$

$R_{\rm H_2}$ can then be solved for analytically, with $\Sigma(R_{\rm H_2})$, $\alpha_{\rm vir}(R_{\rm H_2})$, and related properties following as demonstrated in Section 2.1.

A.2. Power-law Profile with Constant-density Core

We consider a clump following a power-law density profile with a uniform core of radius R_0,

$$\rho(r) = \begin{cases} \rho_c \text{ for } r < \mathrm{R}_0 \\ \rho_c\ x^{-k} \text{ for } r \geqslant \mathrm{R}_0, \end{cases} \tag{A13}$$

where ρ_c is the central density and $x = r/R_0$. From Equation (A1), the mass within r is

$$M(r) = \begin{cases} \pi\rho_c R_0^3\left[\frac{4}{3}x^3\right] \text{ for } r < R_0 \\ \pi\rho_c R_0^3\Pi_1(r) \text{ for } r \geqslant R_0, \end{cases} \tag{A14}$$

where $\Pi_1(r) = \left[\frac{4}{3-k}\left(x^{3-k} - \frac{k}{3}\right)\right]$. From Equation (A2), the gravitational term is

$$\Omega_G(r) \equiv \begin{cases} -\frac{16}{15}\pi^2 G\rho_c^2 R_0^5 x^5 \text{ for } r < R_0 \\ -\pi^2 G\rho_c^2 R_0^5\Pi_2(r) \text{ for } r \geqslant R_0, \end{cases} \tag{A15}$$

where

$$\Pi_2(r) = \begin{cases} \frac{16}{3-k}\left(\frac{x^{5-2k}-1}{5-2k} + \frac{k(1-x^{2-k})}{6-3k} + \frac{3-k}{15}\right) \text{ for } k \neq 2 \\ \frac{16}{3-k}\left(\frac{x^{5-2k}-1}{5-2k} - \frac{k\ln(x)}{3} + \frac{3-k}{15}\right) \text{ for } k = 2. \end{cases} \tag{A16}$$

From Equation (A3), the kinetic term is

$$\Omega_K(r) = \begin{cases} 2\pi\rho_c R_0^3 x^3\sigma_v^2(r) \text{ for } r < R_0 \\ \frac{3}{2}\pi\rho_c R_0^3\Pi_1(r)\sigma_v^2(r) \text{ for } r \geqslant R_0. \end{cases} \tag{A17}$$

Requiring $2\Omega_K = -\Omega_G$, we then define the virial mass

$$M_{\rm vir}(r) = \begin{cases} \frac{5R_0\sigma_v^2(r)}{G}x \text{ for } r < R_0 \\ \frac{3R_0\sigma_v^2(r)}{G}\frac{\Pi_1(r)^2}{\Pi_2(r)} \text{ for } r \geqslant R_0, \end{cases} \tag{A18}$$

and finally the virial parameter as

$$\alpha_{\rm vir}(r) = \begin{cases} \frac{15\sigma_v^2(r)}{4\pi\rho_c G R_0^2}\frac{1}{x^2} \text{ for } r < R_0 \\ \frac{3\sigma_v^2(r)}{\pi\rho_c G R_0^2}\frac{\Pi_1(r)}{\Pi_2(r)} \text{ for } r \geqslant R_0. \end{cases} \tag{A19}$$

We cast this profile in terms of f_{DG} as defined in Equation (1), such that

$$f_{\rm DG} = \begin{cases} 1 - \left(\dfrac{3-k}{3} \dfrac{(R_{\rm CO}/R_0)^3}{(R_{\rm H_2}/R_0)^{(3-k)} - \dfrac{k}{3}} \right) & \text{for } R_{\rm CO} < R_0 \\ 1 - \left(\dfrac{(R_{\rm CO}/R_0)^{(3-k)} - \dfrac{k}{3}}{(R_{\rm H_2}/R_0)^{(3-k)} - \dfrac{k}{3}} \right) & \text{for } R_{\rm CO} \geqslant R_0, \end{cases} \tag{A20}$$

assuming $R_{\rm H_2} > R_0$. $R_{\rm H_2}$ can then be solved for analytically, with $\Sigma(R_{\rm H_2})$, $\alpha_{\rm vir}(R_{\rm H_2})$, and related properties following.

A.3. Plummer Density Profile

We consider a clump following a Plummer density profile,

$$\rho(r) = \rho_c \left(\frac{1}{\sqrt{x^2+1}} \right)^{\eta}, \tag{A21}$$

where ρ_c is the central density, $x = r/R_0$, R_0 is the radius of the central core, and η is the index of the power law at large radii. From Equation (A1), the mass within r is

$$M(r) = \pi \rho_c R_0^3 P_1(r), \tag{A22}$$

where

$$P_1(r) = \begin{cases} 4(x - \arctan(x)) \text{ for } \eta = 2 \\ 2\left(\arctan(x) - \dfrac{x}{x^2+1} \right) \text{ for } \eta = 4. \end{cases} \tag{A23}$$

From Equation (A2), the gravitational term can be written as

$$\Omega_G(r) = -\pi^2 G \rho_c^2 R_0^5 P_2(r) = -\frac{GM(r)^2}{R_0} \frac{P_2(r)}{P_1(r)^2}, \tag{A24}$$

where

$$P_2(r) = \begin{cases} 16\left(x - \arctan(x) - \displaystyle\int_0^x \frac{x' \arctan(x')}{x'^2+1} \mathrm{d}x' \right) \text{ for } \eta = 2 \\ \arctan(x) + \dfrac{x - 4\arctan(x)}{x^2+1} + \dfrac{2x}{(x^2+1)^2} \text{ for } \eta = 4. \end{cases} \tag{A25}$$

From Equation (A3), the kinetic term is

$$\Omega_K(r) = \frac{3}{2} \pi \rho_c R_0^3 \sigma_v^2(r) P_1(r). \tag{A26}$$

We can then derive the virial mass through requiring $2\Omega_K = -\Omega_G$,

$$M_{\rm vir}(r) = \frac{3 R_0 \sigma_v^2(r)}{G} \frac{P_1(r)^2}{P_2(r)}, \tag{A27}$$

and finally the virial parameter

$$\alpha_{\rm vir}(r) = \frac{3\sigma_v^2(r)}{\pi \rho_c G R_0^2} \frac{P_1(r)}{P_2(r)}. \tag{A28}$$

We adapt this profile into f_{DG} as defined in Equation (1), such that

$$f_{\rm DG} = \begin{cases} 1 - \left(\dfrac{\dfrac{R_{\rm CO}}{R_0} - \arctan(R_{\rm CO}/R_0)}{\dfrac{R_{\rm H_2}}{R_0} - \arctan(R_{\rm H_2}/R_0)} \right) \text{ for } \eta = 2 \\ 1 - \left(\dfrac{\arctan(R_{\rm CO}/R_0) - \dfrac{(R_{\rm CO}/R_0)}{(R_{\rm CO}/R_0)^2+1}}{\arctan(R_{\rm H_2}/R_0) - \dfrac{(R_{\rm H_2}/R_0)}{(R_{\rm H_2}/R_0)^2+1}} \right) \text{ for } \eta = 4. \end{cases} \tag{A29}$$

$R_{\rm H_2}$ can then be solved for numerically to obtain estimates of $\Sigma(R_{\rm H_2})$, $\alpha_{\rm vir}(R_{\rm H_2})$, and related properties.

ORCID iDs

Theo J. O'Neill https://orcid.org/0000-0003-4852-6485
Rémy Indebetouw https://orcid.org/0000-0002-4663-6827
Alberto D. Bolatto https://orcid.org/0000-0002-5480-5686
Suzanne C. Madden https://orcid.org/0000-0003-3229-2899
Tony Wong https://orcid.org/0000-0002-7759-0585

References

Abdo, A. A., Ackermann, M., Ajello, M., et al. 2010, ApJ, 710, 133
Arzoumanian, D., André, P., Didelon, P., et al. 2011, A&A, 529, L6
Astropy Collaboration, Price-Whelan, A. M., Sipőcz, B. M., et al. 2018, AJ, 156, 123
Astropy Collaboration, Robitaille, T. P., Tollerud, E. J., et al. 2013, A&A, 558, A33
Ballesteros-Paredes, J., Hartmann, L. W., Vázquez-Semadeni, E., Heitsch, F., & Zamora-Avilés, M. A. 2011, MNRAS, 411, 65
Bertoldi, F., & McKee, C. F. 1992, ApJ, 395, 140
Bertram, E., Klessen, R. S., & Glover, S. C. O. 2015, MNRAS, 451, 196
Bigiel, F., Leroy, A. K., Walter, F., et al. 2011, ApJL, 730, L13
Bolatto, A. D., Leroy, A. K., Jameson, K., et al. 2011, ApJ, 741, 12
Bolatto, A. D., Leroy, A. K., Rosolowsky, E., Walter, F., & Blitz, L. 2008, ApJ, 686, 948
Bolatto, A. D., Wolfire, M., & Leroy, A. K. 2013, ARA&A, 51, 207
Brunt, C. M., Heyer, M. H., & Mac Low, M. M. 2009, A&A, 504, 883
Caselli, P., Benson, P. J., Myers, P. C., & Tafalla, M. 2002, ApJ, 572, 238
Caselli, P., & Myers, P. C. 1995, ApJ, 446, 665
Chen, H. H.-H., Offner, S. S. R., Pineda, J. E., et al. 2020, arXiv:2006.07325
Chen, H. H.-H., Pineda, J. E., Goodman, A. A., et al. 2019, ApJ, 877, 93
Chevance, M., Kruijssen, J. M. D., Vazquez-Semadeni, E., et al. 2020, SSRv, 216, 50
Chevance, M., Madden, S. C., Fischer, C., et al. 2020, MNRAS, 494, 5279
Clark, P. C., & Glover, S. C. O. 2015, MNRAS, 452, 2057
de los Reyes, M. A. C., & Aennicutt, R. C. J. 2019, ApJ, 872, 16
Dessauges-Zavadsky, M., Richard, J., Combes, F., et al. 2019, NatAs, 3, 1115
Dobbs, C. L. 2015, MNRAS, 447, 3390
Field, G. B., Blackman, E. G., & Keto, E. R. 2011, MNRAS, 416, 710
Fukui, Y., Kawamura, A., Minamidani, T., et al. 2008, ApJS, 178, 56
Galametz, M., Madden, S., Galliano, F., et al. 2009, A&A, 508, 645
Girichidis, P., Federrath, C., Banerjee, R., & Klessen, R. S. 2011, MNRAS, 413, 2741
Glover, S. C. O., & Clark, P. C. 2012, MNRAS, 421, 9
Glover, S. C. O., Federrath, C., Mac Low, M. M., & Klessen, R. S. 2010, MNRAS, 404, 2
Glover, S. C. O., & Mac Low, M.-M. 2011, MNRAS, 412, 337
Gong, M., Ostriker, E. C., & Kim, C.-G. 2018, ApJ, 858, 16
Gong, M., Ostriker, E. C., Kim, C.-G., & Kim, J.-G. 2020, ApJ, 903, 142
Goodman, A. A., Barranco, J. A., Wilner, D. J., & Heyer, M. H. 1998, ApJ, 504, 223
Gordon, K. D., Meixner, M., Meade, M., et al. 2011, AJ, 142, 102

Grenier, I. A., Casandjian, J.-M., & Terrier, R. 2005, Sci, 307, 1292
Harris, C. R., Millman, K. J., van der Walt, S. J., et al. 2020, Natur, 585, 357
Heyer, M., Krawczyk, C., Duval, J., & Jackson, J. M. 2009, ApJ, 699, 1092
Heyer, M. H., & Brunt, C. M. 2004, ApJL, 615, L45
Hughes, A., Meidt, S. E., Colombo, D., et al. 2013, ApJ, 779, 46
Hughes, A., Wong, T., Ott, J., et al. 2010, MNRAS, 406, 2065
Hunter, J. D. 2007, CSE, 9, 90
Jameson, K. E., Bolatto, A. D., Leroy, A. K., et al. 2016, ApJ, 825, 12
Jameson, K. E., Bolatto, A. D., Wolfire, M., et al. 2018, ApJ, 853, 111
Juvela, M., Malinen, J., Montillaud, J., et al. 2018, A&A, 614, A83
Kalari, V. M., Rubio, M., Saldaño, H. P., & Bolatto, A. D. 2020, MNRAS, 499, 2534
Kauffmann, J., Pillai, T., & Goldsmith, P. F. 2013, ApJ, 779, 185
Kennicutt, R. C. J., Calzetti, D., Walter, F., et al. 2007, ApJ, 671, 333
Kim, S., Rosolowsky, E., Lee, Y., et al. 2007, ApJS, 171, 419
Krumholz, M. R. 2012, ApJ, 759, 9
Langer, W. D., Velusamy, T., Pineda, J. L., Willacy, K., & Goldsmith, P. F. 2014, A&A, 561, A122
Larson, R. B. 1981, MNRAS, 194, 809
Lee, E. J., Chang, P., & Murray, N. 2015, ApJ, 800, 49
Lee, M.-Y., Stanimirović, S., Douglas, K. A., et al. 2012, ApJ, 748, 75
Leroy, A. K., Bolatto, A., Bot, C., et al. 2009, ApJ, 702, 352
Leroy, A. K., Schinnerer, E., Hughes, A., et al. 2021, ApJS, 257, 43
Leroy, A. K., Walter, F., Brinks, E., et al. 2008, AJ, 136, 2782
Li, Q., Narayanan, D., Davè, R., & Krumholz, M. R. 2018, ApJ, 869, 73
Lin, Y., Wyrowski, F., Liu, H. B., et al. 2022, A&A, 658, A128
MacLaren, I., Richardson, K. M., & Wolfendale, A. W. 1988, ApJ, 333, 821
Madden, S. C., Cormier, D., Hony, S., et al. 2020, A&A, 643, A141
Madden, S. C., Galliano, F., Jones, A. P., & Sauvage, M. 2006, A&A, 446, 877
Muraoka, K., Homma, A., Onishi, T., et al. 2017, ApJ, 844, 98
Ochsendorf, B. B., Meixner, M., Roman-Duval, J., Rahman, M., & Evans, N. J. 2017, ApJ, 841, 109
Oka, T., Hasegawa, T., Sato, F., et al. 2001, ApJ, 562, 348
Palmeirim, P., André, P., Kirk, J., et al. 2013, A&A, 550, A38
Paradis, D., Dobashi, K., Shimoikura, T., et al. 2012, A&A, 543, A103
Parmentier, G. 2020, ApJ, 893, 32
Parmentier, G., & Pasquali, A. 2020, ApJ, 903, 56
Passot, T., Pouquet, A., & Woodward, P. 1988, A&A, 197, 228
Pattle, K. 2016, MNRAS, 459, 2651
Pineda, J. E., Goodman, A. A., Arce, H. G., et al. 2010, ApJL, 712, L116
Pineda, J. L., Langer, W. D., Velusamy, T., & Goldsmith, P. F. 2013, A&A, 554, A103
Pirogov, L. E. 2009, ARep, 53, 1127
Planck Collaboration, Ade, P. A. R., Aghanim, N., et al. 2011, A&A, 536, A19
Plummer, H. C. 1911, MNRAS, 71, 460
Ridge, N. A., Francesco, J. D., Kirk, H., et al. 2006, AJ, 131, 2921
Rubele, S., Girardi, L., Kerber, L., et al. 2015, MNRAS, 449, 639
Rubio, M., Elmegreen, B. G., Hunter, D. A., et al. 2015, Natur, 525, 218
Saldaño, H. P., Rubio, M., Jameson, K., & Bolatto, A. D. 2018, BAAA, 60, 192
Schneider, N., André, P., Könyves, V., et al. 2013, ApJL, 766, L17
Schruba, A., Kruijssen, J. M. D., & Leroy, A. K. 2019, ApJ, 883, 2
Schruba, A., Leroy, A. K., Kruijssen, J. M. D., et al. 2017, ApJ, 835, 278
Schruba, A., Leroy, A. K., Walter, F., et al. 2012, AJ, 143, 138
Shetty, R., Beaumont, C. N., Burton, M. G., Kelly, B. C., & Klessen, R. S. 2012, MNRAS, 425, 720
Shetty, R., Glover, S. C., Dullemond, C. P., et al. 2011b, MNRAS, 415, 3253
Shetty, R., Glover, S. C., Dullemond, C. P., & Klessen, R. S. 2011a, MNRAS, 412, 1686
Smith, R. J., Glover, S. C. O., Clark, P. C., Klessen, R. S., & Springel, V. 2014, MNRAS, 441, 1628
Solomon, P. M., Rivolo, A. R., Barrett, J., & Yahil, A. 1987, ApJ, 319, 730
Sun, J., Leroy, A. K., Ostriker, E. C., et al. 2020, ApJ, 892, 148
Sun, J., Leroy, A. K., Schruba, A., et al. 2018, ApJ, 860, 172
Szucs, L., Glover, S. C. O., & Klessen, R. S. 2016, MNRAS, 460, 82
Tang, M., Liu, T., Qin, S.-L., et al. 2018, ApJ, 856, 141
Tatematsu, K., Umemoto, T., Kandori, R., & Sekimoto, Y. 2004, ApJ, 606, 333
Traficante, A., Duarte-Cabral, A., Elia, D., et al. 2018, MNRAS, 477, 2220
Valdivia-Mena, M. T., Rubio, M., Bolatto, A. D., Saldaño, H. P., & Verdugo, C. 2020, A&A, 641, A97
Vázquez-Semadeni, E., Palau, A., Ballesteros-Paredes, J., Gómez, G. C., & Zamora-Avilés, M. 2019, MNRAS, 490, 3061
Velusamy, T., Langer, W. D., Pineda, J. L., et al. 2010, A&A, 521, L18
Volgenau, N. H., Mundy, L. G., Looney, L. W., & Welch, W. J. 2006, ApJ, 651, 301
Whitworth, A. P., & Ward-Thompson, D. 2001, ApJ, 547, 317
Wolfire, M. G., Hollenbach, D., & McKee, C. F. 2010, ApJ, 716, 1191
Wong, T., Hughes, A., Fukui, Y., et al. 2009, ApJ, 696, 370
Wong, T., Hughes, A., Tokuda, K., et al. 2019, ApJ, 885, 50
Xu, D., Li, D., Yue, N., & Goldsmith, P. F. 2016, ApJ, 819, 22
Zucker, C., Goodman, A., Alves, J., et al. 2021, ApJ, 919, 35